Polarization contrast neutron imaging of magnetic crystallographic phases

M. Busi [a], E. Polatidis [a], C. Sofras [a, b], P. Boillat [a], A. Ruffo [a], C. Leinenbach [c, b], M. Strobl [a, d, *]

[a] Paul Scherrer Institut, Laboratory for Neutron Scattering and Imaging, 5232 Villigen, Forschungsstrasse 111, Switzerland
[b] École Polytechnique Fédérale de Lausanne, EDMX-Materials Science and Engineering, 1015 Lausanne, Route Cantonale, Switzerland
[c] EMPA - Swiss Federal Laboratories for Materials Science and Technology, 8600 Dübendorf, Ueberlandstrasse 129, Switzerland
[d] Niels Bohr Institute, University of Copenhagen, Blegdamsvej 172100 Copenhagen, Denmark

ARTICLE INFO

ABSTRACT

Non-destructive characterization methods to observe phase transformations and thus, gain insights to transformation mechanisms in representative volumes are key for the development of advanced materials and manufacturing. Conventional methods are constrained to the surface and small sizes, thus, access to the bulk often implies tedious destructive approaches and hinders in-situ observations of phase evolution. In this work, we introduce a non-destructive technique that overcomes key limitations prevailing today for mapping the spatial distribution of magnetic phases in bulk materials. The use of polarized neutrons, being sensitive to sub-percent fractions of ferromagnetic phases and able to penetrate centimeter sized samples, enables micrometer-scale spatial and second-scale time resolutions. We demonstrate ex-situ and in-situ quantitative mapping of magnetic phases, in particular the evolution of martensite induced by uniaxial- and biaxial deformation in metastable 304 steel. The quantitative results obtained during in-situ deformation testing prove polarization contrast neutron imaging to be particularly effective in detecting small fractions of martensite. Especially during early stages of deformation where neutron diffraction, which in contrast does not provide full field spatial resolution, fails. The short exposure times and high sensitivity renders the method well suited for rapid 3D tomographic mapping and/or operando investigations of phase distributions.

© 2022 The Authors. Published by Elsevier Ltd. This is an open access article under the CC BY license (http://creativecommons.org/licenses/by/4.0/).

1. Introduction

Microstructural properties such as solid-state phase transformations and their distribution determine to a large extent the global mechanical properties of materials. It remains critically important to study e.g. the relationship of phase transformation kinetics and relate them with other microstructural properties such as dislocation density evolution, grain size or crystallographic texture to develop experimentally verified constitutive laws for computational tools. The development of such experimentally verified and robust computational tools will accelerate the development and utilization of advanced manufacturing and materials for addressing societal requirements of human welfare, safe and green transportation, sustainable infrastructure and clean energy.

The availability and advancement of characterization techniques remains essential to obtain a fundamental understanding of transformation mechanisms allowing the development of accurate phase transformation models [1].

Deformation or thermally induced martensitic phase transformations in ferrous alloys and steels give rise to important structural and functional properties, such as strength in transformation-induced plasticity (TRIP) steels [1] and shape memory or superelasticity effects in ferrous shape-memory alloys (SMAs) [2]. Their related properties are of particular importance for numerous engineering applications as structural materials in the automotive industry, biomedical industry, civil applications, as actuators etc. In these materials, the initial microstructure contains a fraction, or consists entirely of metastable austenitic face-centered-cubic (FCC) phase that transforms into martensite upon deformation, or during fatigue or cold working. Depending on the chemical composition of the material and the extent of deformation, two different martensitic phases are commonly created under load, the body-centered-cubic (BCC) α'-martensite and/or the hexagonal

---

close-packed (HCP), ε-martensite [3]. Martensite with BCC crystal structure is particularly important as it hardens the material, while good ductility is maintained due to the presence of austenite. As such, an optimum trade-off between strength and ductility can be achieved [4].

Traditional techniques (e.g. optical microscopy, electron microscopy, electron backscatter diffraction, X-ray diffraction, magnetic and ultrasonic measurements) are constrained to the surface or to small-sized material samples (i.e. sub-millimeters) and are, thus, often not representative of the bulk. Access to the bulk implies destructive approaches hindering in-situ observations of phase evolution. Also recently developed advanced synchrotron X-ray techniques such as 3D-XRD [5] and X-ray diffraction contrast tomography [6] that provide unique insights through 3D microstructure maps, are typically limited to small sample volumes. Additional limitations, e.g. the degree of mosaicity, hinders studies of plastically deformed materials. Only neutrons [7−10] and high energy synchrotron X-ray diffraction [11] provide access to bulk microstructures. However, to gain crucial spatially resolved insights to meso-scale phenomena in the bulk of polycrystalline materials, novel neutron imaging methods have been developed continuously throughout past decades. In particular, wavelength resolved diffraction contrast neutron imaging [12,13] has been utilized extensively for 2- and 3- dimensional mapping of phase distributions [8,14−18] and observations of phase evolution [19−21]. Bragg edge imaging of crystalline phase distributions provides spatial resolutions down to a few tens of μm. However, to achieve high resolution and to identify small fractions and subtle changes of phase requires exposure times up to a few hours, depending on the instrumental method deployed [13,22]. However, being able to detect subtle changes and low fractions in-situ and with sufficient resolution is generally of particular relevance, like, for instance, in order to understand the degradation mechanisms in components made of ferrous SMAs, where accumulation of deformation-induced α'-martensite is non reversible and highly undesirable [23].

Here, we introduce a different non-destructive approach that overcomes key limitations prevailing today for mapping the spatial distribution of crystalline phases in bulk materials by being sensitive to sub-percent phase fractions with micrometer-scale spatial and second-scale time resolution. We validate the linear dependence between the measured depolarization coefficient and the magnetic phase fraction using a set of samples consisting of different mixtures of ferromagnetic α-iron powder with paramagnetic austenitic 316L stainless steel powder. Subsequently, we demonstrate ex-situ and in-situ mapping of ferromagnetic phases, in particular the evolution of strain induced martensitic phase in metastable 304 steel induced under uniaxial- and biaxial deformation. The method capitalizes on the high sensitivity of the neutron's magnetic moment μ_n to magnetic fields and structures, as well as the high transmission capability of neutrons, rendering it a unique assessment tool for a wide range of conventional and advanced materials of high technological relevance. The spatial resolution based on pixel sizes of 50×50 μm^2 is orders of magnitude better than in conventional neutron diffraction [13], while leveraging the integral flux of a broad wavelength range, i.e. a white beam, implies the method to outperform advanced wavelength resolved diffraction contrast imaging methods by orders of magnitude in efficiency, i.e. time resolution and sensitivity.

2. Method

A polarized incident white neutron beam is depolarized when interacting with the microstructure of magnetic domains in a ferromagnetic material [24,25]. Thus, analyzing the beam polarization after interacting with a sample enables detecting ferromagnetic phases in the material. While wavelength dispersive transmission measurements were used in the past and enable the characterization of average domain sizes [24,25], our spatially resolved technique with a highly intense white beam provides detailed images of the distribution of phases exhibiting ferromagnetism. The method, which has been similarly applied in the past to study the Curie temperature distribution in heterogeneous alloys [26,27], requires to equip a neutron imaging beamline that enables spatially resolved measurements through e.g. a pinhole geometry, with neutron polarization and polarization analyses capabilities [28,29]. The incident beam with a thermal or cold wavelength spectrum is polarized by a neutron spin filter (NSF), typically a polarizing supermirror device utilizing the different refractive index of the spin-up and spin-down components of an unpolarized beam in a strong magnetic field to reflect one and absorb the other component in a subsequent absorber layer coating on the backside of the mirror. However, polarized ^{3}He can serve as NSF as well. The high polarization of the neutrons transmitting the NSF is preserved in the beamline by a guide field aligned parallel to the transmitted polarization and ideally spanning the length up to the second NSF, the polarization analyzer. A sample to be measured is placed between the two NSFs as close as possible to the analyzer, without interfering with its magnetic stray field, in order to achieve the best possible resolution on the subsequent imaging detector. The deterioration of spatial resolution by the extended sample to detector distance implied by the need of the analyzer can be compensated by beam collimation, which has to be tailored to the experimental needs to not excessively sacrifice flux and, thus, efficiency. In order to measure the local beam polarization $P(x, y)$, which is characterized by the ratio:

$$P = \frac{I_\uparrow - I_\downarrow}{I_\uparrow + I_\downarrow} \tag{1}$$

an adiabatic fast passage π spin flipper [30] is installed upstream of the sample and allows to subsequently record both the spin-up intensity $I_\uparrow(x, y)$ and the spin-down intensity $I_\downarrow(x, y)$. Without a sample in the beam the measured polarization $P_0(x, y)$ is close to unity throughout an image. When the neutrons spin, however, they experience magnetic interactions with magnetic fields characteristic of a sample under investigation, they undergo Larmor precessions with the frequency $\omega_L = \gamma \mathbf{B}$ according to the strength and orientation of the magnetic field $\mathbf{B}$ of e.g. magnetic domains and depending on the time spent in the field. $\gamma = 4\pi\mu_n/h$ is the gyromagnetic factor of the neutron with h being the Planck constant [31]. The time spent in the field, and thus precessing, depends on the extension of the field, like the domain size d and sample thickness t as well as on the neutron velocity v and therefore the wavelength λ of the neutron (Eq. (4)). This leads to depolarization effects and, hence, a resulting polarization $P(x, y)$ depending on local magnetic structures and phases. In analogy to the Beer Lambert law of attenuation:

$$I(x, y) = I_0(x, y)e^{-\mu(x,y)t(x,y)}, \tag{2}$$

where $I_0 = I_{0\uparrow} + I_{0\downarrow}$ is the incident intensity and $I = I_\uparrow + I_\downarrow$ is the transmitted intensity and μ is the linear attenuation coefficient, the transmitted polarization can, to a first approximation, be expressed as:

$$P(x, y) = P_0(x, y)e^{-\eta(x,y)t(x,y)}, \tag{3}$$

where the depolarization coefficient η for a ferromagnetic material with randomly oriented domains is written as [24]:

$$\eta = \frac{\log (P/P_0)}{t} = \frac{\gamma^2 B^2 d}{3 v^2} = \frac{1}{3} \left(\frac{4\pi \, \mu_n \lambda m}{h^2} B \right) \qquad (4)$$

3. Experimental section

Polarization contrast neutron imaging (PNI) measurements were carried out at the BOA beamline [32] of the Paul Scherrer Institut (Villigen, Switzerland). BOA is characterized by a cold neutron spectrum, with a peak wavelength of 2.8 Å and a mean wavelength of 3.8 Å, and is permanently equipped with a multi-channel polarizing-bender unit [32] between the cold source and the beamline pinhole of 40×40 mm^2 at the exit from the source monolith. The instrument was further equipped with an adiabatic π-spin flipper, a magnetic guide field and a 40×40 mm^2 super-mirror NSF used as spin analyzer (Fig. 1a)). The average instrumental white beam polarization P_0 of the setup was measured to have been around 86%. The neutron imaging detector comprised of a 200 µm thick scintillator screen (LiF/ZnS(Ag)) and an optical Andor iKon-M CCD camera (1024×1024 pixels) with a Zeiss MAKRO-PLANAR 2/100 mm ZF.2 objective lens. The magnification of the lens was such to achieve an effective pixel size of 65 µm, implying a camera field of view of 67×67 mm^2. The effective field of view is, however, limited by the spin analyzer dimension.

A set of samples consisted of different mixtures of ferromagnetic α-iron powder with paramagnetic austenitic 316L stainless steel powder. The 316L powder (FCC structure) has a particle size distribution of 15−45 µm (purchased from Carpenter Additive, USA), while the pure Fe powder (BCC structure) has a particle size range of 6−8 µm (purchased from Goodfellow, UK). The powder mixtures were contained in quartz cuvettes with sample thickness of 2 and 5 mm. Pure iron powder (with BCC crystal structure) was mixed at ratios of 0, 0.5, 1, 1.5 and 2 wt. % with 316L powder (with FCC crystal structure). The distribution of martensite resulting from the TRIP effect induced by uniaxial and biaxial deformation tests was investigated in a set of cruciform-shaped specimens of commercial hot-rolled AISI 304 (EN.1.4301) stainless steel purchased from SAUTER EDELSTAHL AG, Switzerland. Fig. 1b) shows a schematic of the cruciform sample geometry and indicates the directions of the load paths with respect to the hot-rolling direction of the steel plates during manufacturing. The field of view defined by the spin analyzer is indicated. The sample thickness gradually decreases from 8 mm at the gripping parts to an uniform 2 mm thick circular

section with 24 mm diameter at the center of the sample, more information is provided in [33]. The deformation tests were carried out using the biaxial deformation rig of the neutron diffraction instrument POLDI at SINQ, Switzerland [34]. The samples investigated were an as received specimen (AR), two samples deformed under uniaxial tension (S1, S2) and one sample that had been subjected to non-proportional multiaxial loading (S3). S1 and S2 were loaded along the axis of the cruciform shape that was parallel to the hot-rolling direction, with up to 35 kN (S1) and 40 kN (S2), reaching a maximum equivalent strain of 12.7% and 21.4% respectively. S3 underwent loading with a force ratio of 49 kN:59 kN between the two orthogonal axes, reaching a maximum equivalent strain of 39%. The von Mises equivalent strain was calculated by definition of the analysis software of the implemented digital image correlation system (GOM Aramis®).

Furthermore, an in-situ uniaxial tensile deformation experiment was performed using an additively manufactured dogbone sample of 304L stainless steel with 60 mm length and 6 mm gauge diameter. The sample was additively manufactured using a pre-alloyed, gas atomized 304L stainless steel powder, with a particle size distribution of 15−45 µm (purchased from Metalalpine GmbH, Austria). The adopted manufacturing technique was laser powder bed fusion (LPBF) using a Sisma MySint 100 printer with a laser spot size of 55 µm. The process parameters conveying a laser power of 175 W, a hatching distance of 83 µm, a scanning speed of 600 mm/s and a layer thickness of 30 µm were suited to achieve a proper material density. During the experiment the sample was loaded stepwise slightly above to the yield point, i.e. at 375 MPa (YP) and at 0.5%, 1%, 2%, 4%, 6% engineering strain before unloading back to 0 MPa.

PNI measurements were performed with exposure times of 60 s per image. Open beam and sample images were recorded always for both spin-up and spin-down configuration. All images were corrected by dark-current background measurements without exposure and reduced first to map the background corrected transmission I/I_0 and polarization ratio P/P_0 and subsequently according to Eqs. (2) and (3) in order to achieve spatially resolved maps of μ and η, respectively. In the case of the glass cuvettes used as sample containers, one of these has been measured in empty state, in order to correct also for its contribution to the signal, in particular the attenuation signal. Three samples in glass cuvettes could be exposed simultaneously, due to the spatially resolved character of the measurements.

To additionally verify the presence of ferrite and martensite optically in the vicinity of the surface the samples were ground
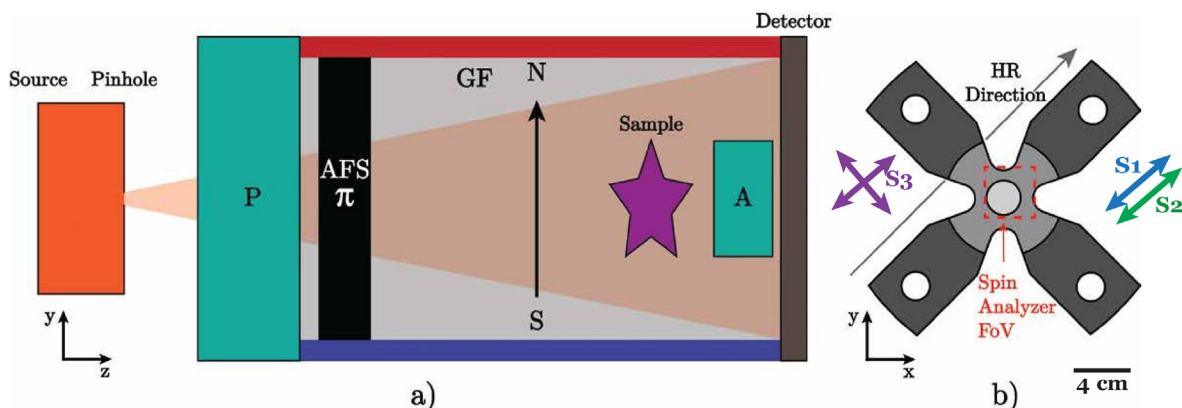

Fig. 1. a) Schematic of the polarization neutron imaging setup, comprised of a polarizer NSF (P), an adiabatic π spin flipper (ASF), a magnetic guide field (GF) and a spin analyzer NSF (A). b) Sketch of the cruciform sample and the field of view projected by the spin analyzer, as well as the direction of the steel plate hot-rolling direction and the multiaxial load paths.

with 1200 grit SiC sandpaper and then electropolished for 12 s with a 16:3:1 (by volume) ethanol, glycerol and perchloric acid solution at 42 V. The samples were then tint etched using Beraha's tint etchant for stainless steels with 20 mL HCl, 100 mL water, 2.4 g ammonium bifluoride and 0.6 g potassium metabisulfite. The samples were immersed in the solution for approximately 30 s. The optical micrographs were obtained using polarized light conditions on a Leica DMRX optical microscope equipped with a JENOPTIK ProgResTM GRYPHAXTM Speed XT core 3 camera.

4. Results

4.1. FCC/BCC powder mixtures

The results of the reference measurements with the FCC/BCC powder mixtures are displayed in Fig. 2. Fig. 2a) shows the measured transmission and polarization ratio radiographs for the powder mixtures in the 2 mm cuvettes as well as an empty cuvette that was used for correcting the transmission and depolarization for the contribution of the glass material. The transmission and polarization ratio for each of the powders and different cuvette thicknesses, obtained by averaging for the whole sample area, are plotted against the nominal BCC weight fraction in Fig. 2b). The influence of the sample thickness in the two quantities is high-lighted by the strong offset in the individual pair of curves. Nevertheless, the results confirm a linear dependence of the de-polarization coefficient on the phase fraction of the ferromagnetic alpha iron. This is illustrated in Fig. 2c) where the linear attenuation and depolarization coefficients averaged over the sample areas are plotted against the nominal weight fraction of the magnetic BCC iron phase. This procedure yields linear attenuation coefficients that are the same within a maximum 6% error for all the samples measured. These results are as expected since the bulk density and the total attenuation cross sections of the powders should not change significantly for different concentrations of BCC powder. With respect to the linear depolarization coefficient, the results further underline the high sensitivity of the method to detect low phase fractions down to sub-percent resolution in the case of iron. This high sensitivity in addition reveals that the commercial austenitic powder contains ferromagnetic phases, which is apparent by the depolarization measured for the allegedly 100%

FCC phase sample. Indeed, a simple check with a permanent magnet confirms that the powder is lightly magnetic, possibly due to the existence of hematite on the surface of the powder particles. A first degree polynomial fit, $\eta(BCC) = m\,BCC + \eta_0$, of the depolarization coefficient versus the nominal BCC weight fraction yields very similar values for the different sample thicknesses, with slope m equal to 1.21 cm^{-1} and 1.16 cm^{-1} for the 2 mm and 5 mm thickness respectively and the offset η_0, due to the ferromagnetic phases in the austenitic powder, equal to 1.10 cm^{-1} and 1.14 cm^{-1}. Furthermore, the reference measurements reveal insufficient mixing of the powders as agglomerations of ferromagnetic iron phase in some regions of the sample become obvious in the de-polarization images (Fig. 2a)).

4.2. Cruciform sample load tests

Fig. 3 shows the radiographic maps of the ferritic phase fraction for the four different cruciform samples. The ferritic phase fraction has been calculated by first obtaining the linear depolarization coefficient as for the powder mixtures. A thickness map has been obtained from the attenuation contrast map, to correct for varying thickness in the sample. For quantification, the resulting images are scaled according to a reference point of high martensite fraction probed by neutron diffraction [8]. In the AR sample (i.e. prior to deformation), a low ferritic phase fraction can be observed with streaks along one of the cruciform arms' directions. Deformation results in strain-induced martensitic phase transformation at the center of the cruciform sample S1 (a) with phase fraction up to 5%, as well as some martensite transformation at locations where stresses concentrate (b). Upon further uniaxial straining (sample S2), the fraction of the strain-induced martensite increases in the whole region (c) into a more uniform distribution of phase fraction. After biaxial loading with a 49 kN: 59 kN load ratio between the cruciform axes (S3), the strain-induced martensite fraction is observed to be higher than in the two uniaxially loaded samples (S1 and S2). The resulting martensite phase fraction map, shows het-erogeneous martensite concentrations that are associated with the stress localization in cruciform samples, as previously reported using neutron diffraction and/or diffraction imaging [8,22]. The central region of sample S3 was measured by neutron diffraction by sampling an area of 3.8×3.8 mm^2, which is schematically shown in
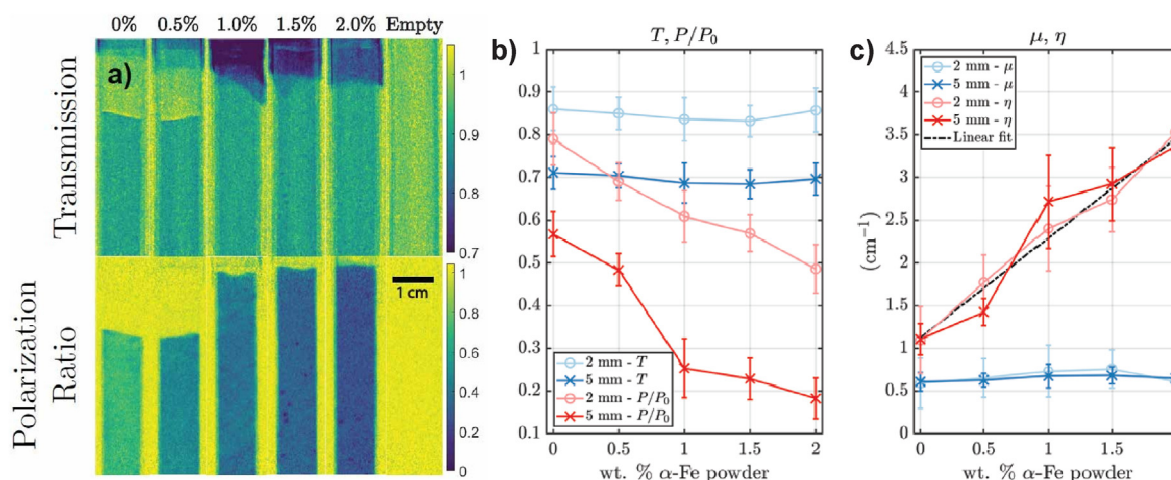

Fig. 2. a) Transmission and polarization ratio radiographs of the powder mixtures in the 2 mm thick cuvettes, as well as one empty cuvette. b) Average transmission (blue colors) and polarization ratio (red colors) for each of the five powder mixtures in the 2 mm thick (light colors and round marker) and the 5 mm thick (dark colors and cross marker) cuvettes. c) The linear attenuation and depolarization coefficients corresponding to the b) panel. Note that the same color and marker layout applies. In dashed black is shown a line fit using the depolarization coefficient profiles.
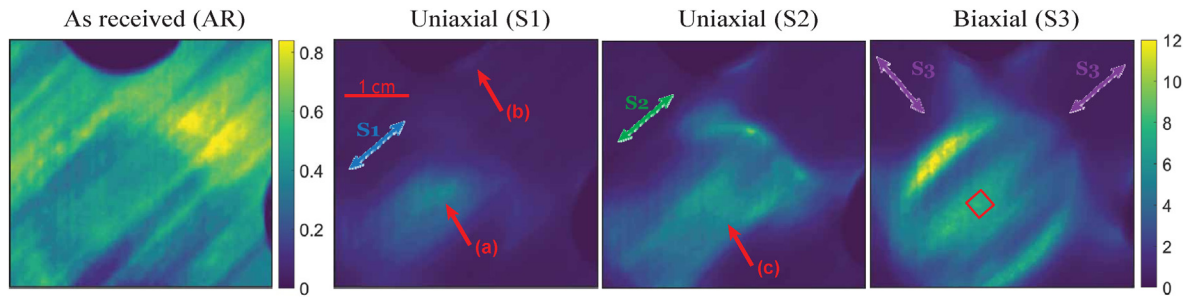
Fig. 3. Spatial mapping of the ferritic phase fraction (%) of the central part of the cruciform samples as it goes from as received (AR) condition, through two uniaxial loads (S1 and S2) and finally, a 49 kN: 59 kN biaxial loading (S3). The load directions are identical to those in Fig. 1b). Note the different phase fraction amplitude range in the color bars. The marked red box shows the 3.8×3.8 mm² region used for the calibration, corresponding to the neutron diffraction gauge volume.

Fig. 3. The phase fraction obtained by neutron diffraction, i.e. 6.8% in the center of the cruciform S3, was used as a reference for calibrating the depolarization coefficient, averaged in the exact same area of 3.8×3.8 mm² in the center of S3. It should be noted that PNI does not distinguish between magnetic phases having different crystal structures unlike diffraction methods.

As aforementioned, in the low phase fraction regime, visible for the AR cruciform sample, the presence of strongly directional ferritic bands is observed, which are aligned parallel to the rolling direction. These are assumed to be caused by the presence of δ-ferrite, due to their relatively low ferritic phase fraction and their strikingly strong directional shape. δ-Ferrite is known to form in hot-rolled austenitic steel plates, and studies report that an austenitic matrix can contain up to 9% of δ-ferrite [35].

The structural direction of the δ-ferrite corresponds to the direction of the hot-rolling, and this was validated by repeating the PNI measurement after rotating the sample 90° around the beam direction axis. A corresponding rotation of the δ-ferrite was observed confirming this was not an effect produced by background image artifacts. Fig. 4 shows an optical microscope measurement of a part of the cruciform sample after grinding the outer surface of the sheet, followed by polishing and etching. In the panel a), and especially in the highlighted area the presence of a band of δ-ferrite, aligned with the hot-rolling direction, in the microstructure is confirmed. As such, the superimposition of all the δ-ferrites can be revealed using PNI.

4.3. In-situ load test

Fig. 5 shows the radiographs of the dogbone sample according to several steps of tensile loading. The linear attenuation and depolarization coefficients have been calculated using Eqs. (3) and (4).

It can be observed from the attenuation radiographs that the tensile load leads to an elongation and thus thinning of the sample from an initial diameter of 6 mm down to a final diameter of 5.8 mm for the 6% engineering strain load. However, the attenuation contrast does not exhibit significant contrast changes for the different stress load steps. In contrast, the depolarization contrast shows a gradual increase of strain-induced martensite, as the stress load increases, which becomes highly visible at the 2% engineering strain. At 6% engineering strain, the depolarization ratio reaches its maximum. The evolution of the strain-induced martensite was also measured with neutron diffraction at POLDI with a twin specimen, up to engineering strain of 20%, as shown in Fig. 5c). Utilizing the calibration of the previous sample S3 it can be seen that the initial stages of deformation match well between the two methods, and PNI is able to capture very well the transformation behavior up to strains of 6% engineering strain. At such low fractions neutron diffraction struggles to obtain reliable values, whereas PNI is especially sensitive in capturing the initial stages of the transformation.

5. Conclusion

Polarization contrast neutron imaging has been applied to study the presence of magnetic phases in iron-based materials and in metastable austenitic samples that partially transform to martensite upon deformation. The method introduces a multimodal approach for the analysis of the material microstructural properties through the complementary and simultaneous measurement of the attenuation of the neutron beam and the depolarization caused by the existence of magnetic phases. Experimentally, the method is based on highly efficient measurements in radiographic mode and it is seen to be exceptionally
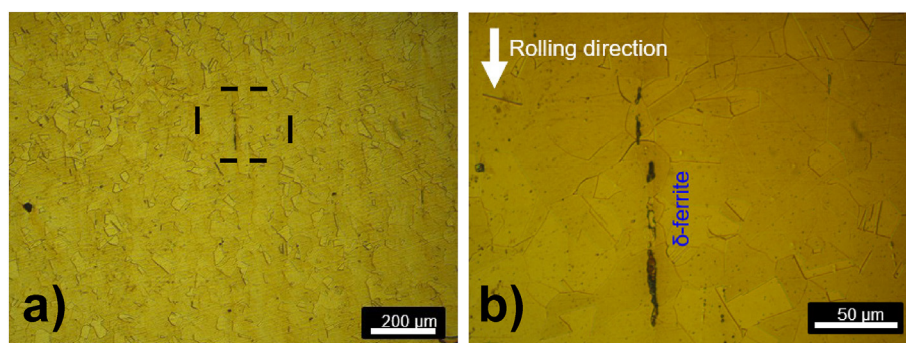

Fig. 4. a) Optical microscope image of one of the cruciform samples in a region far from where the martensitic transformation occurs an additional layer has removed and the surface has been polished. b) 4x magnification of the dashed-line noted region.
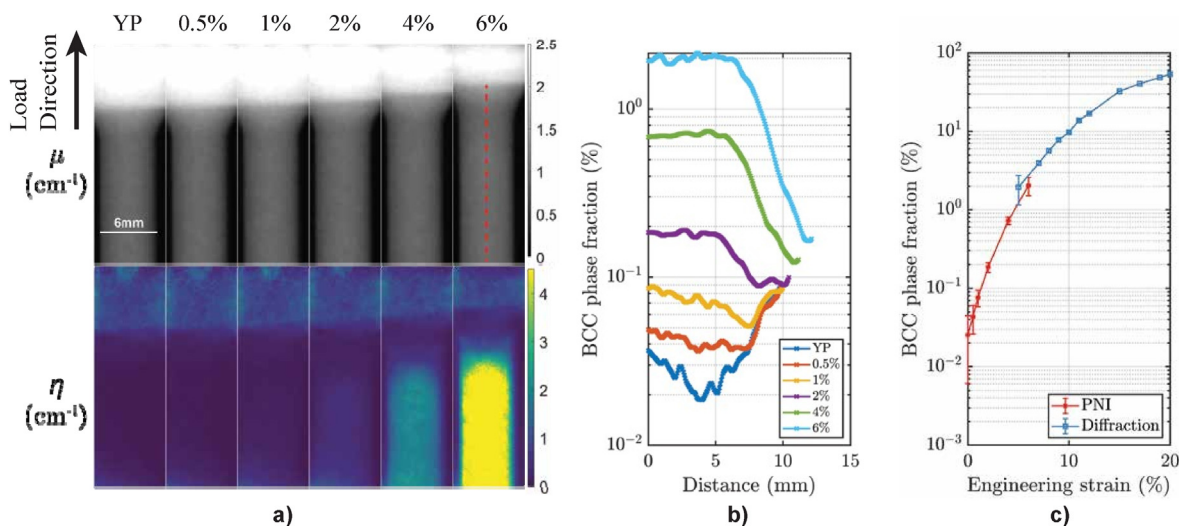
Fig. 5. a) Linear attenuation (μ) and depolarization (η) coefficient contrast radiographs of the dogbone sample at the yield point (YP) and following different steps of tensile rig load. Note that the load direction during the tests was vertical.

sensitive in observing low ferritic/martensitic phase fractions, which are often obscured when using conventional diffraction techniques, as for instance the presence of δ-ferrite needles in hot rolled steels. Unlike diffraction-based methods, depolarization imaging is not affected by grain size (e.g. poor grain statistics) or crystallographic texture in the material. In particular, the method offers good spatial resolution and allows to capture phase distributions of full scale bulk samples. The quantitative results during an in situ deformation test of a metastable austenitic steel agree well when related to conventional measurements, while PNI is particularly effective in detecting small fractions of martensite, during early stages of deformation. Finally, the method requires exposure times of only a few tens of seconds to a few minutes, making it promising in particular for time-resolved studies, e.g. to follow the evolution of the crystalline phase transformations in response to external loads, but also for tomographic measurements with many angular projections and correspondingly high spatial resolution.

Declaration of competing interest

The authors declare that they have no known competing financial interests or personal relationships that could have appeared to influence the work reported in this paper.

Data availability

Data will be made available on request.

Acknowledgements

References

[1] M. Militzer, A synchrotron look at steel, Science 298 (5595) (2002) 975−976.
[2] J. Ma, I. Karaman, Expanding the repertoire of shape memory alloys, Science 327 (5972) (2010) 1468−1469.
[3] G. Olson, M. Cohen, Kinetics of strain-induced martensitic nucleation, Metall. Trans. A 6 (4) (1975) 791−795.
[4] M. Soleimani, A. Kalhor, H. Mirzadeh, Transformation-induced plasticity (TRIP) in advanced steels: a review, Mater. Sci. Eng., A 795 (2020), 140023.
[5] H.F. Poulsen, Three-dimensional X-Ray Diffraction Microscopy: Mapping Polycrystals and Their Dynamics, Volume 205, Springer Science & Business Media, 2004.
[6] A. King, G. Johnson, D. Engelberg, W. Ludwig, J. Marrow, Observations of intergranular stress corrosion cracking in a grain-mapped polycrystal, Science 321 (5887) (2008) 382−385.
[7] S. Harjo, N. Tsuchida, J. Abe, W. Gong, Martensite phase stress and the strengthening mechanism in TRIP steel by neutron diffraction, Sci. Rep. 7 (1) (2017) 1−11.
[8] E. Polatidis, M. Morgano, F. Malamud, M. Bacak, T. Panzner, H. Van Swygenhoven, M. Strobl, Neutron diffraction and diffraction contrast imaging for mapping the trip effect under load path change, Materials 13 (6) (2020) 1450.
[9] D.-d. Ma, P. Yang, X.-F. Gu, Y. Onuki, S. Sato, In-situ neutron diffraction investigation on the martensite transformation, texture evolution and martensite reversion in high manganese TRIP steel, Mater. Char. 163 (2020), 110244.
[10] W. Woo, J. Jeong, D.-K. Kim, C. Lee, S.-H. Choi, J.-Y. Suh, S. Lee, S. Harjo, T. Kawasaki, Stacking fault energy analyses of additively manufactured stainless steel 316L and CrCoNi medium entropy alloy using in situ neutron diffraction, Sci. Rep. 10 (1) (2020) 1−15.
[11] R. Blonde, E. Jimenez-Melero, L. Zhao, J. Wright, E. Brück, S. Van der Zwaag, N. Van Dijk, High-energy X-ray diffraction study on the temperature-dependent mechanical stability of retained austenite in low-alloyed TRIP steels, Acta Mater. 60 (2) (2012) 565−577.
[12] J. Santisteban, L. Edwards, A. Steuwer, P. Withers, Time-of-flight neutron transmission diffraction, J. Appl. Crystallogr. 34 (3) (2001) 289−297.
[13] R. Woracek, J. Santisteban, A. Fedrigo, M. Strobl, Diffraction in neutron imaging—a review, Nucl. Instrum. Methods Phys. Res. Sect. A Accel. Spectrom. Detect. Assoc. Equip. 878 (2018) 141−158.
[14] R. Woracek, D. Penumadu, N. Kardjilov, A. Hilger, M. Boin, J. Banhart, I. Manke, 3D mapping of crystallographic phase distribution using energy-selective neutron tomography, Adv. Mater. 26 (24) (2014) 4069−4073.
[15] M.G. Makowska, M. Strobl, N. Kardjilov, H.L. Frandsen, I. Manke, M. Morgano, M.E. Lacatusu, S. De Angelis, E.M. Lauridsen, L.T. Kuhn, Investigating phase behavior and structural changes in NiO/Ni-YSZ composite with mono-chromatic in-situ 2D and static 3D neutron imaging, Phys. B Condens. Matter 551 (2018) 24−28.
[16] M. Bacak, J. Valsecchi, J. Čapek, E. Polatidis, A. Kaestner, A. Arabi-Hashemi, I. Kruk, C. Leinenbach, A. Long, A. Tremsin, et al., Neutron dark-field imaging applied to porosity and deformation-induced phase transitions in additively manufactured steels, Mater. Des. 195 (2020), 109009.
[17] W. Woo, J. Kim, E.-Y. Kim, S.-H. Choi, V. Em, D.S. Hussey, Multi- scale analyses of constituent phases in a trip-assisted duplex stainless steel by electron backscatter diffraction, in situ neutron diffraction, and energy selective neutron imaging, Scripta Mater. 158 (2019) 105−109.
[18] H. Sato, T. Sato, Y. Shiota, T. Kamiyama, A.S. Tremsin, M. Ohnuma, Y. Kiyanagi, Relation between Vickers hardness and Bragg-edge broadening in quenched steel rods observed by pulsed neutron transmission imaging, Mater. Trans. 56 (8) (2015) 1147−1152.
[19] M.G. Makowska, M. Strobl, E.M. Lauridsen, S. Kabra, W. Kockelmann,

A. Tremsin, H.L. Frandsen, L. Theil Kuhn, In situ time-of-flight neutron imaging of NiO−YSZ anode support reduction under influence of stress, J. Appl. Crystallogr. 49 (5) (2016) 1674−1681.

[20] M.G. Makowska, L.T. Kuhn, H.L. Frandsen, E.M. Lauridsen, S. De Angelis, L.N. Cleemann, M. Morgano, P. Trtik, M. Strobl, Coupling between creep and redox behavior in nickel-yttria stabilized zirconia observed in-situ by monochromatic neutron imaging, J. Power Sources 340 (2017) 167−175.

[21] E. Dabah, B. Pfretzschner, T. Schaupp, N. Kardjilov, I. Manke, M. Boin, R. Woracek, A. Griesche, Time-resolved Bragg-edge neutron radiography for observing martensitic phase transformation from austenitized super martensitic steel, J. Mater. Sci. 52 (6) (2017) 3490−3496.

[22] M. Busi, J. Čapek, E. Polatidis, J. Hovind, P. Boillat, A.S. Tremsin, W. Kockelmann, M. Strobl, Frame overlap Bragg edge imaging, Sci. Rep. 10 (1) (2020) 1−10.

[23] W. Jang, Q. Gu, J. Van Humbeeck, L. Delaey, Microscopic observation of γ-phase and ε-and α'-martensite in Fe − Mn− Si-based shape memory alloys, Mater. Char. 34 (2) (1995) 67−72.

[24] O. Halpern, T. Holstein, On the passage of neutrons through ferromagnets, Phys. Rev. 59 (12) (1941) 960.

[25] M. Burgy, D. Hughes, J. Wallace, R. Heller, W. Woolf, Double transmission and depolarization of neutrons, Phys. Rev. 80 (6) (1950) 953.

[26] M. Schulz, A. Neubauer, S. Masalovich, M. Mühlbauer, E. Calzada, B. Schillinger, C. Pfleiderer, P. Böni, Towards a tomographic reconstruction of neutron depolarization data, in: Journal of Physics: Conference Series, ume 211, IOP Publishing, 2010, 012025.

[27] M. Schulz, A. Neubauer, P. Böni, C. Pfleiderer, Neutron depolarization imaging of the hydrostatic pressure dependence of inhomogeneous ferromagnets, Appl. Phys. Lett. 108 (20) (2016), 202402.

[28] N. Kardjilov, I. Manke, M. Strobl, A. Hilger, W. Treimer, M. Meissner, T. Krist, J. Banhart, Three-dimensional imaging of magnetic fields with polarized neutrons, Nat. Phys. 4 (5) (2008) 399−403.

[29] M. Strobl, Future prospects of imaging at spallation neutron sources, Nucl. Instrum. Methods Phys. Res. Sect. A Accel. Spectrom. Detect. Assoc. Equip. 604 (3) (2009) 646−652.

[30] E. Babcock, A. Petoukhov, J. Chastagnier, D. Jullien, E. Lelievre-Berna, K. Andersen, R. Georgii, S. Masalovich, S. Boag, C. Frost, et al., AFP flipper devices: polarized 3He spin flipper and shorter wavelength neutron flipper, Phys. B Condens. Matter 397 (1−2) (2007) 172−175.

[31] M. Strobl, H. Heimonen, S. Schmidt, M. Sales, N. Kardjilov, A. Hilger, I. Manke, T. Shinohara, J. Valsecchi, Polarization measurements in neutron imaging, J. Phys. Appl. Phys. 52 (12) (2019) 123001.

[32] M. Morgano, S. Peetermans, E. Lehmann, T. Panzner, U. Filges, Neutron imaging options at the BOA beamline at Paul Scherrer Institut, Nucl. Instrum. Methods Phys. Res. Sect. A Accel. Spectrom. Detect. Assoc. Equip. 754 (2014) 46−56.

[33] E. Polatidis, M. Šmíd, W.-N. Hsu, M. Kubenova, J. Čapek, T. Panzner, H. Van Swygenhoven, The interplay between deformation mechanisms in austenitic 304 steel during uniaxial and equibiaxial loading, Mater. Sci. Eng., A 764 (2019), 138222.

[34] S. Van Petegem, J. Wagner, T. Panzner, M. Upadhyay, T. Trang, H. Van Swygenhoven, In-situ neutron diffraction during biaxial deformation, Acta Mater. 105 (2016) 404−416.

[35] F. Czerwinski, A. Brodtka, J. Cho, J. Szpunar, A. Zielinska-Lipiec, J. Sun- woo, A role of δ-ferrite in edge-crack formation during hot-rolling of austenitic stainless steels, Scripta Mater. 37 (8) (1997).